ADVANCED ENERGY MATERIALS
www.advenergymat.de

Plasmon-Driven Nitrogen Photoreduction to Ammonia Using Silica-Encapsulated Au Nanostar/TiO_2 Nanohybrids

Yoel Negrín-Montecelo, Ana Sousa-Castillo, Noel Cardeñoso-Garrido, Lucía Guillade, Lucas V. Besteiro, Margarita Vázquez-González, Ramón A. Alvarez-Puebla, Begoña Puértolas, and Miguel A. Correa-Duarte**

Plasmon-induced photocatalysis has gained traction as a promising means to efficiently drive chemical reactions using light. In particular, photocatalytic N_2 reduction emerges as a sustainable route to produce ammonia, a key starting material in the manufacture of nitrogen-rich fertilizers and a potential energy vector. Here, various Au nanoparticle morphologies combined with a TiO_2 semiconductor are initially screened, and Au nanostar is identified as the most efficient morphology. Encasing this material within a mesoporous silica shell improved their stability and selectivity to ammonia formation, eliminating the need for hole scavengers. Advanced characterization including TEM and *operando* SERS spectroscopy together with the evaluation of the material in the presence of optical filters and probes reveal that the superior performance originates from the injection of excited "hot" charge carriers from the plasmonic material to the semiconductor, driving N_2 reduction to NH_3 under visible light. The wavelength-dependence experiments demonstrate a synergistic interaction between gold interband transitions and plasmonic effects, combined with the TiO_2 semiconductor, which enhances catalytic performance across the spectrum. Importantly, hot holes generated at the plasmonic sites oxidize water into oxygen and subsequently to nitrates, maintaining charge balance in the photocatalyst. This dual functionality ensures effective charge circulation and sustainable performance across multiple cycles.

1. Introduction

Despite its severe operating conditions, associated energy consumption, and environmental concerns, the manufacture of nitrogen-rich fertilizers still relies heavily on producing ammonia (NH_3) on centralized chemical plants via the Haber-Bosch process. A more sustainable emerging scheme considers the on-site production of carbon-neutral fertilizers at ambient conditions in photocatalytic reactors powered by sunlight.[1] Among the different strategies proposed to boost the N_2 reduction ability of conventional photocatalysts, the incorporation of plasmonic nanomaterials is gaining widespread interest owing to their unique optical tunability and ability to improve the efficiency and selectivity of many chemical transformations.[2–4] Conducting nanoparticles (NPs), such as Ag, Au, or Cu support local surface plasmon resonances (LSPRs), produced when the incoming electromagnetic field excites resonant collective electronic oscillations of the metal.[5] LSPRs mediate N_2 reduction via plasmon-assisted photocatalysis, the latter targeting the selective cleavage of the N≡N bond to produce NH_3. To tackle this, most of the reported systems are based on hybrid materials in which the photocatalytic component is combined with a plasmonic resonator (generally Au).[6] The occurrence of anion (N, C, O, S) vacancies on the photocatalytic semiconductor promotes N_2 fixation, owing to their ability to bear excess electronic charge and unsaturated metal centers for the activation, and subsequent

Y. Negrín-Montecelo, R. A. Alvarez-Puebla
Department of Physical and Inorganic Chemistry
Universitat Rovira i Virgili
Tarragona 43007, Spain

A. Sousa-Castillo, N. Cardeñoso-Garrido, L. Guillade, L. V. Besteiro, M. Vázquez-González, B. Puértolas, M. A. Correa-Duarte
CINBIO
Universidade de Vigo
Vigo 36310, Spain
E-mail: begona.puertolas@uvigo.es; macorrea@uvigo.es

R. A. Alvarez-Puebla
ICREA—Institució Catalana de Recerca i Estudis Avançats
Barcelona 08010, Spain

M. A. Correa-Duarte
Southern Galicia Institute of Health Research (IISGS)
Vigo 36310, Spain

M. A. Correa-Duarte
Biomedical Research Networking Center for Mental Health (CIBERSAM)
Vigo 36310, Spain

The ORCID identification number(s) for the author(s) of this article can be found under https://doi.org/10.1002/aenm.202501526

DOI: 10.1002/aenm.202501526

reduction of N_2 to NH_3.[7] Complementary, the injection of hot electrons generated on the plasmonic metal into the conduction band of the semiconductor or directly into the N_2 molecule, boosts the NH_3 formation. As a result, the NH_3 formation rate increases when compared to the performance of the bare semiconductor.[8]

Tuning the frequency of the LSPR modes of plasmonic NPs according to the targeted application strongly depends on the NP composition, shape, size, organization, and surrounding environment.[9–11] The combined choice of composition and geometry of the NP controls its optical characteristics as a plasmonic resonator and permits the design of nanoantennas that absorb light at different wavelengths in the UV-to-IR range.[12] Different plasmonic geometries not only influence the spectral response of the resonator, but also its scattering-to-absorption ratio[13] and the spatial distribution of their enhanced electric near fields, with regions of large curvature such as the tips of nanorods and nanostars supporting "hot spots" with strong electric fields.[14–16] These can enhance optical processes near such regions,[17,18] and are also responsible for increasing the rate of excitation of high-energy carriers that can contribute to photoredox reactions,[19,20] favoring nanostructures with sharp features in a photocatalytic context.[21,22] Bare metal NPs are poorly suited to the harsh conditions required for many practical applications, which can induce aggregation, etching, or other undesired effects,[23] thus severely undermining all efforts to tailor the plasmonic particle properties. To improve their manipulation and facilitate their applicability, the synthesis of individual plasmonic colloids encapsulated in both dense and mesoporous silica shells has become a prominent approach.[24] In the context of catalysis, this strategy has been exploited to identify the underlying photoactivation mechanisms, i.e., the local enhancement of the electromagnetic field, the injection of charge carriers, the increase of temperature produced through photoheating, or the radiative relaxation, for diverse photo(electro)catalysis applications. Although these mechanisms can coexist in a given system and can thus participate simultaneously in the same photochemical reaction, the adequate engineering of the silica dielectric coating can balance their relative relevance or even suppress some of them, as happens in many cases with the injection of hot carriers upon the introduction of the silica shell.[25]

Herein, we assess the impact of the Au NP morphology in SiO_2/Au/TiO_2 hybrids in the visible light-driven N_2 reduction to NH_3 in the absence of hole scavengers. Having identified Au nanostars (AuNST) as the best performer, we explore the effect of introducing a mesoporous silica shell on the stability when subjecting the hybrid to consecutive reaction cycles. Catalytic assessment of the materials with optical filters and probes enabled us to elucidate the mechanism behind the observed catalytic performance.

2. Results and Discussion

2.1. Structural and Optical Characterization

It is well established that plasmonic nanoparticles generate hot electrons upon light irradiation, and the efficiency of this process is strongly influenced by factors such as nanoparticle shape, composition, and excitation wavelength. To enable a comparative analysis, plasmonic Au NPs with three distinct morphologies were synthesized.[22,26] These NPs include: nanospheres (AuNSP) with a diameter of 14 ± 1 nm, AuNST with a core diameter of 35 ± 5 nm and spike length of 9 ± 1 nm, and nanorods (AuNR) with a longitudinal dimension of 58 ± 5 nm and a transversal length of 17 ± 2 nm (**Figure 1a**; Figure S1, Supporting Information). The distinct absorption signatures of these three morphologies are clearly illustrated in Figure 1a. AuNSP exhibit a single and narrow absorption band with a peak centered at 520 nm, characteristic of such nanostructures. On the other hand, anisotropic particles exhibit more complex spectral profiles. For AuNST, optical extinction spectroscopy reveals bimodal resonance bands in the visible and NIR regions, attributed to structural heterogeneity. The core size produces a shoulder at 530 nm, while the spikes are centered at 650 nm. Similarly, AuNR display distinct signals with transverse and longitudinal resonances at 520 and 790 nm, respectively.

The plasmonic NPs were assembled onto SiO_2 particles (480 nm in diameter) through electrostatic interactions.[22] The resulting nanostructure was coated with a layer of TiO_2 (anatase) NPs with an average diameter of 5 nm, forming SiO_2/TiO_2 photocatalysts (Figure 1b). XPS analysis of the TiO_2 nanoparticles evidences the doublet Ti $2p_{3/2}$ (binding energy 458.5 eV) and Ti $2p_{1/2}$ (binding energy 464.2 eV) that indicate that titanium in the nanoparticle surface is mostly as TiO_2 (Figure S2, Supporting Information). The applied layer-by-layer assembly allows for precise control over the deposition of both the plasmonic photosensitizers and the large bandgap semiconductor materials onto the silica templates. Furthermore, a highly uniform distribution of these components was achieved on the bead surfaces, creating a consistent Au–TiO_2 interface across the samples. Importantly, for comparison purposes, each catalyst was synthesized with identical amounts of Au and TiO_2.[22,26] These loadings were fixed to the optimal amount of metal component needed for maximum photosensitization of the semiconductor and was supported by the results obtained by Inductively Coupled Plasma Optical Emission spectroscopy (ICP-OES, Table S1, Supporting Information).[27]

In contrast with the spectral signatures of the plasmonic Au NPs, the UV-visible spectra of the corresponding composites exhibit a strong absorption band at lower wavelengths (Figure 1b). This effect is attributed to the high UV absorption of TiO_2, combined with significant scattering from the SiO_2 support. Despite this, LSPR signatures of the Au NPs remain discernible, exhibiting a slight red shift as expected. This shift is a result of the increased effective refractive index surrounding the plasmonic NPs due to the presence of SiO_2 and TiO_2.[22,28,29] Tauc plots from diffuse reflectance spectra (DRS) of the SiO_2/TiO_2 and SiO_2/AuNST/TiO_2 hybrids revealed similar band gap values, i.e., 3.31 and 3.25 eV, respectively (Figure S3, Supporting Information).

As already known, the distinct absorption signatures of these nanohybrids are anticipated to significantly improve their photocatalytic activity due to the varying electromagnetic field enhancements linked to each morphology.[30–32] However, as such, these structures proved to be unstable after several photocatalytic cycles (vide infra). To address this issue, a 10 nm mesoporous silica layer was applied as a protective coating (**Figure 2a**). Subsequently, the SiO_2/AuNST/TiO_2/mSiO_2 nanoarchitectures

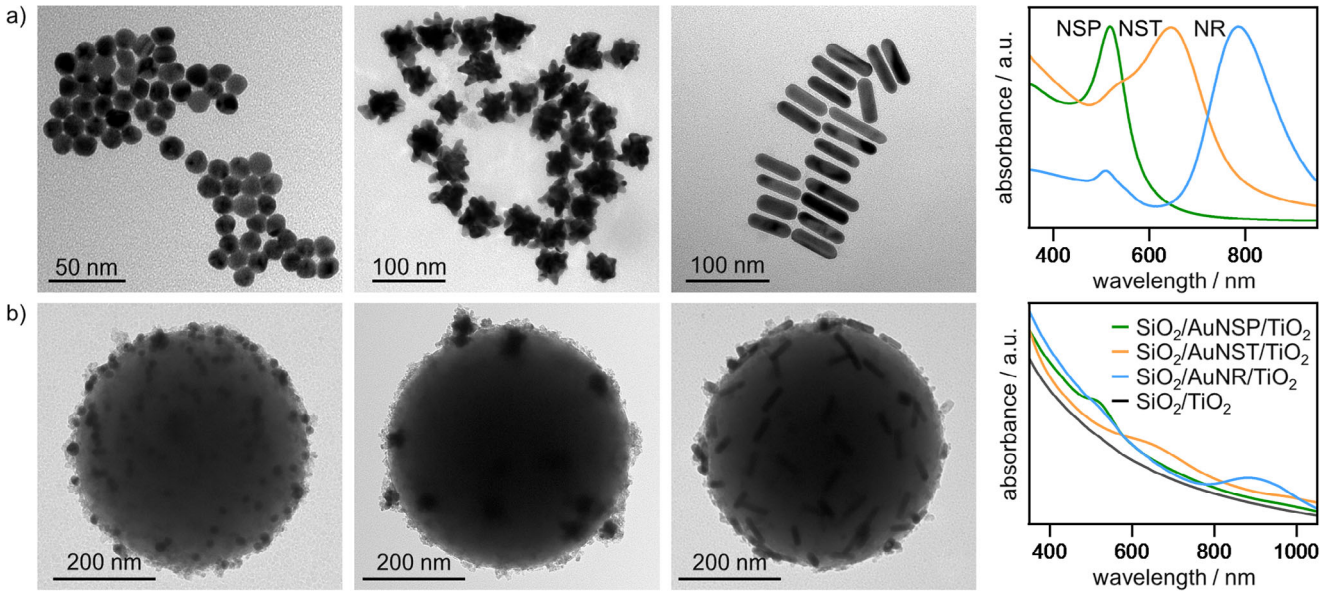

Figure 1. a) TEM micrographs and extinction spectra of the AuNSP, AuNST, and AuNR. b) TEM micrographs of the hybrid SiO_2/AuNSP/TiO_2, SiO_2/AuNST/TiO_2, and SiO_2/AuNR/TiO_2, and their corresponding extinction spectra.

underwent a plasma cleaning process to remove surfactants and organic compounds used in the layer-by-layer assembly. This treatment ensures that reactants can access the AuTiO_2 nanostructure through the pore network during subsequent photocatalytic reactions.[33,34] The high resolution TEM (HRTEM) images in Figure 2a (right) reveal the crystalline lattice of the TiO_2 nanoparticles on a AuNST, all surrounded by an ≈10 nm SiO_2 coating layer. Additionally, scanning transmission electron microscopy in high-angle annular dark field (STEM-HAADF) imaging, combined with energy-dispersive spectroscopy (EDS) analysis (Figure 2b), confirms the presence of the SiO_2 protective layer around the hybrid structure.

2.2. Photocatalytic Assessment in the N_2 Reduction (NRR)

A series of experiments was carried out to identify the most efficient Au nanoparticle morphology in different Au/TiO_2 nanohybrids for photocatalytic NRR activity in the absence of hole scavengers (**Figure 3**; Table S2, Supporting Information). As shown in Figure S4 (Supporting Information), the SiO_2/TiO_2 nanoarchitecture exhibited an activity of 5.8 ± 1.3 μmol g_{cat}^{-1} h^{-1}. This residual activity is primarily due to the limited portion of the solar spectrum, i.e., UV light that possesses sufficient energy to induce electron transitions between the valence and conduction bands of the semiconductor.[22,35] In contrast, the incorporation of Au

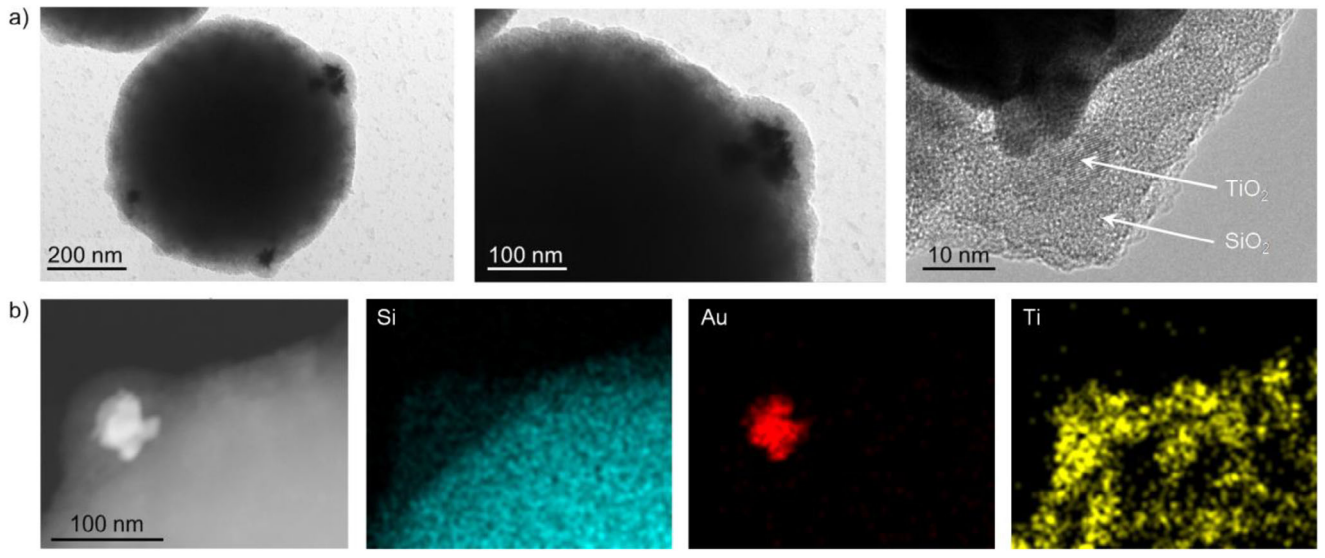

Figure 2. a) High resolution TEM and b) scanning transmission electron micrograph and corresponding elemental maps of Si, Au, and Ti of the SiO_2/AuNST/TiO_2/mSiO_2 sample.

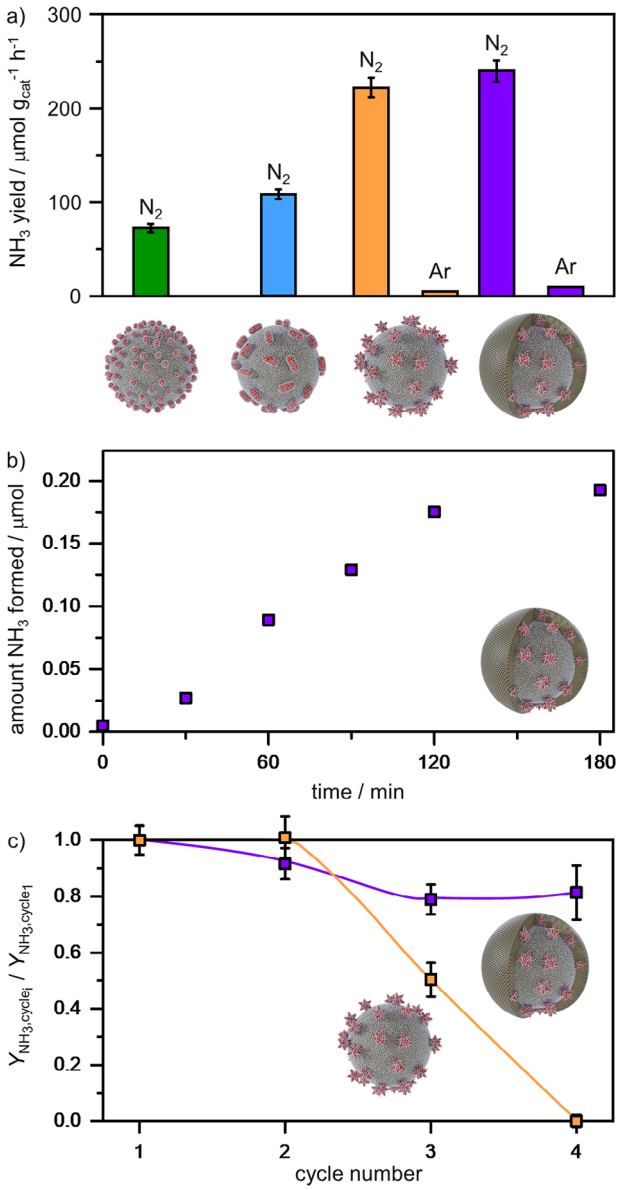

Figure 3. a) NH_3 yield of the SiO_2/AuNSP/TiO_2, SiO_2/AuNR/TiO_2, SiO_2/AuNST/TiO_2, and SiO_2/AuNST/TiO_2/mSiO_2 hybrids in the presence of N_2 and/or Ar. b) Time evolution of the NH_3 formation using SiO_2/AuNST/TiO_2/mSiO_2 as catalyst. c) NH_3 yield upon 4 consecutive photocatalytic cycles for the SiO_2/AuNST/TiO_2 and SiO_2/AuNST/TiO_2/mSiO_2 samples using the first approach for the stability assessment (see Supporting Information for details). Reaction conditions: m_{cat} = 1 mg, $V_{reactor}$ = 3 mL, T = 25°C, t = 1 h per cycle. Wavelength range = 350–2400 nm.

NPs into the system resulted in an increased NH_3 yield, which is attributed to the enhanced number of plasmon-driven catalytic sites.[3,36] This synergy between plasmonic nanoantennas and the TiO_2 nanoparticles suggests that the N_2 reduction occurs primarily at the TiO_2 sites, while the plasmonic structures serve both as oxidation sites as previously demonstrated by the photodegradation of RhB via reactive oxygen species (ROS) created by the oxidation of water[37] and, as it is commonly attributed, as nanoantennas collecting more efficiently the impinging radiant energy. Specifically, the SiO_2/TiO_2 assemblies with AuNSP achieved an NH_3 production rate of 72.1 ± 4.2 μmol g_{cat}^{-1} h^{-1}, while the incorporation of AuNR lead to slightly higher efficiency (109.3 ± 5.5 μmol g_{cat}^{-1} h^{-1}). Remarkably, when AuNST were used as the photosensitizing material, the performance doubled compared to AuNR, reaching 221 ± 10.5 μmol g_{cat}^{-1} h^{-1} under the same experimental conditions. This exceptional performance is attributed to the sharp spikes of the nanoestructure, which generates "hot spots".[2,22,33,38] These hot spots enhance charge injection by significantly amplifying the local electromagnetic fields at the tips of the star-shaped particles. Furthermore, the quasi-spherical symmetry of the AuNST render their optical response largely independent of the polarization of incident light. As a result, nanostar-shaped structures offer an optimal geometry for promoting efficient hot electron transfer to the semiconductor, thereby facilitating the generation of electron–hole pairs that drive redox reactions.[22]

We validated the sensitivity of the colorimetric method for detecting ammonia in aqueous media by comparison with ^1H NMR, using maleic acid as an internal standard under both N_2 and Ar atmospheres. The results closely aligned with those obtained via the indophenol blue method (Figure S5, Supporting Information), indicating that both techniques are suitable for quantitative analysis in these systems and reaction conditions. Furthermore, control experiments using the AuNST plasmonic photosensitizer in an Ar atmosphere instead of N_2 showed negligible NH_3 production, confirming that NH_3 is primarily derived from N_2 reduction (Figure 3a). Additionally, the potential formation of side products, such as hydrazine (N_2H_4) and hydrogen (H_2), was investigated using the Watt and Chrisp method and gas chromatography (GC), respectively.[39] The UV data presented in Figure S6 (Supporting Information) confirms that no N_2H_4 was formed during the photocatalytic reaction. Moreover, negligible H_2 formation was detected by the GC measurements using a thermal conductivity detector (TCD) after the first and the fourth cycle, i.e., 11.59 and 16.34 μmol g_{cat}^{-1} h^{-1}, respectively, which demonstrates the superior selectivity (87%) to NH_3 formation of the SiO_2/AuNST/TiO_2/mSiO_2 hybrid (Figure S7, Supporting Information).

The formation of NH_3 was monitored using operando SERS spectroscopy (**Figure 4a**). At the initial time point (Figure 4a), the spectrum exhibited the typical SERS signature of liquid water. In contrast to gas-phase water, which has C_{2v} molecular symmetry and is characterized by two stretching vibrations at 3651 cm^{-1} (symmetric, a_2 symmetry species) and 3755 cm^{-1} (antisymmetric, b_1 symmetry species), liquid water displays additional features. These include a pronounced band at 3450 cm^{-1}, arising from the combined contributions of free symmetric and antisymmetric O–H stretching vibrations, and another at 3200 cm^{-1}, associated with O–H stretching involved in hydrogen bonding.[40] It is well established that the relative intensity of the 3200 cm^{-1} band decreases as the concentration of ionic species in solution increases.[41] However, in the present study, no significant variation in the relative intensities between the 3450 and 3200 cm^{-1} bands was detected during the catalytic process. This observation likely reflects the low concentration of ammonium ions in close proximity to the surface. Nevertheless, the presence of hydrogenated nitrogen species is evidenced by the appearance

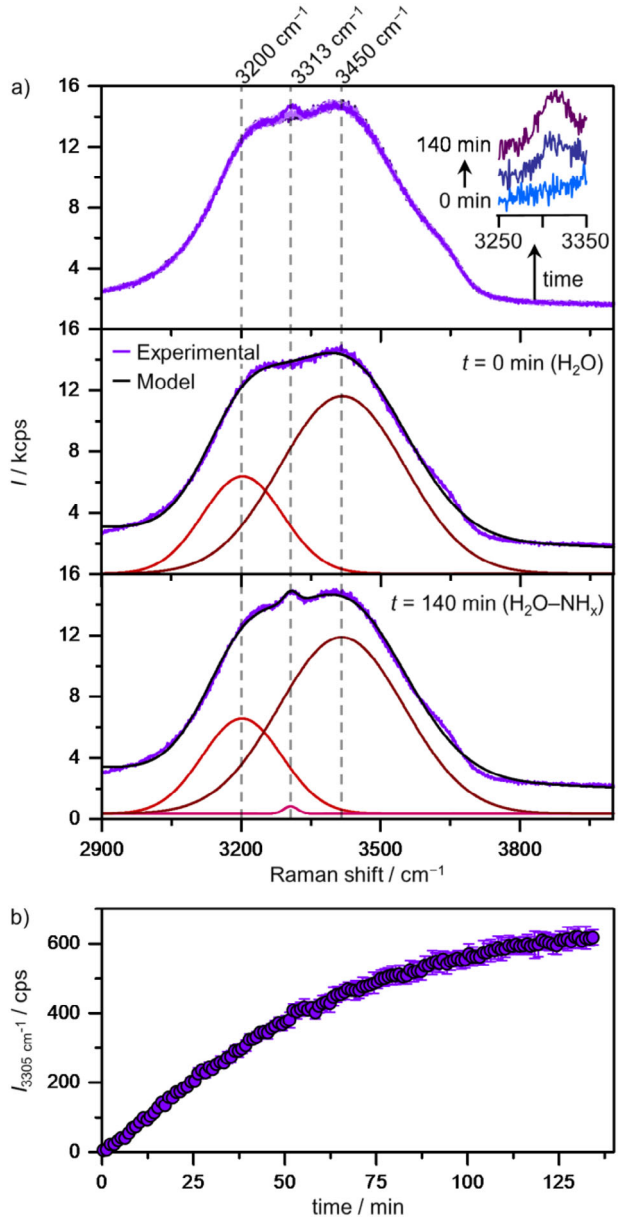

Figure 4. a) *Operando* SERS spectra acquired directly from the reaction vessel (top panel, inset: evolution with time of the spectra in the 3250-3350 cm^{-1} range) and SERS spectrum at the initial reaction time (t = 0 min, middle panel) and after 140 min of reaction (bottom panel) along with their deconvolution. b) Time-dependent representation of the intensity of the deconvoluted band at 3313 cm^{-1}, attributed to the bending vibration of an NH_3–NH_3 dimer.

of new peaks between the two water bands (Figure 4a, time 140 min). A detailed deconvolution of the spectra demonstrated an excellent fit to a three-band model, comprising the 3200 and 3450 cm^{-1} bands attributed to hydrogen-bonded and free water, respectively, along with an additional feature at 3313 cm^{-1}. The band at 3313 cm^{-1} can be confidently assigned to the N–H stretching of NH_3–NH_3 interactions, in agreement with previously reported vibrational data.[42] The simultaneous emergence of these feature supports the formation and accumulation of ammonia in the vicinity of the photocatalytic surface under *operando* conditions. The temporal evolution of this N–H stretching contribution, shown in Figure 4b, reveals a gradual increase in NH_3 production over time, reaching a plateau after approximately two hours, which is in line with the time evolution of the NH_3 formation compiled in Figure 3b. This trend underscores the progressive nature of the catalytic reaction and its stabilization at steady-state conditions. To investigate the potential formation of intermediate species during the reaction, extended acquisition spectra were collected in the range of 600–1700 cm^{-1} (Figure S8, Supporting Information) at reaction times of 0 and 75 min. Comparative analysis of these spectra revealed the emergence of a new vibrational band at 1132 cm^{-1}, along with a shoulder at 880 cm^{-1}. Spectral deconvolution of these regions confirmed the presence of distinct peaks at 1132 and 884 cm^{-1}, which were assigned to the N—N single bond stretching mode and N–N–H deformation, respectively.[43] These findings align with prior studies,[44,45] supporting an associative reaction mechanism for the conversion of N_2 to NH_3. The stability of the photocatalyst is a crucial factor in evaluating its performance. Therefore, we conducted four consecutive catalytic cycles over the SiO_2/AuNST/TiO_2 and SiO_2/AuNST/TiO_2/mSiO_2 nanohybrids, and the results are shown in Figure 3c. Under identical photocatalytic conditions, SiO_2/AuNST/TiO_2 showed a significant decline of its photocatalytic activity whereas SiO_2/AuNST/TiO_2/mSiO_2 proved to be stable. These results indicate that the hybrid nanoarchitecture lacks structural integrity without the protective mesoporous silica layer. TEM images reveal that both the AuNST and TiO_2 detach from the silica template (Figure S8, Supporting Information). In contrast, when an insulating mesoporous silica shell is employed, the photocatalyst remains stable after six cycles (Figures S9 and S10, Supporting Information) and the photoactivity of SiO_2/AuNST/TiO_2/mSiO_2 is slightly improved, resulting in an NH_3 production rate of 240 ± 12.4 μmol g_{cat}^{-1} h^{-1}, which surpasses most of the reported results related to plasmon-assisted photocatalytic N_2 reduction in the absence of hole scavengers (Table S3, Supporting Information).

As postulated in previous studies, the plasmonic activation of a large bandgap semiconductor in aqueous solution leads to the formation of reactive oxygen species (ROS) through the oxidative or reductive path with water and oxygen.[46] In this context, two ROS molecules have been identified as the most relevant species: the hydroxyl radical ($OH^{\cdot}$), as a result of the combination of H_2O molecules with holes; and the superoxide radical (O_2^{-}), as a result of the reduction of the O_2 dissolved in the medium with the generated electrons.[37,47] We conducted control experiments to identify these species and to shed light on the mechanism responsible for the photoreduction of N_2. First, we assessed the formation of the hydroxyl radical ($OH^{\cdot}$) by using the transformation of terephthalic acid (TA) into the fluorescent product 2-hydroxyterephthalic acid (2-HTA) (**Figure** 5a and Figure S11, Supporting Information). Second, we evaluate the superoxide radical formation (O_2^{-}) following the transformation of Nitro Blue tetrazolium (NBT) into its formazan form (Figure 5b; Figure S12, Supporting Information). In the case of the photocatalytic experiments in the presence of O_2, the detection of these molecules is positive and in concordance with the results published in previous studies (dotted lines, Figure 5a,b).[37] However, in the presence of N_2, we were not able to detect $OH^{\cdot}$ or

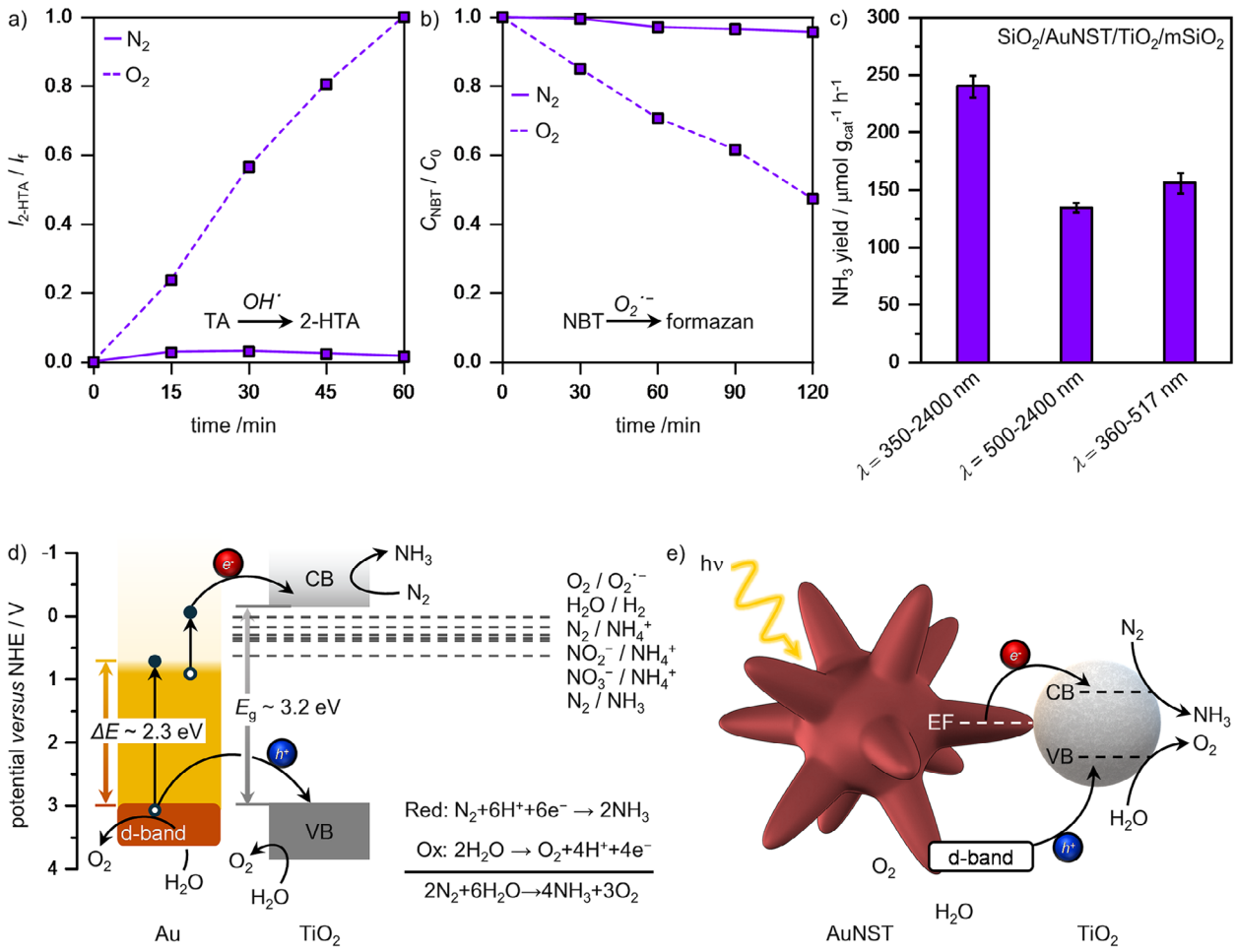

Figure 5. a) Detection of OH˙ by fluorescence spectroscopy through the formation of 2HTA. b) Detection of O_2^- by its reaction with NBT by absorption spectroscopy. The solid and dotted lines represent the phototransformation of the molecules in the presence of N_2 or O_2, respectively over the SiO_2/AuNS/TiO_2/mSiO_2 photocatalyst. c) Photocatalytic results of the SiO_2/AuNS/TiO_2/mSiO_2 sample obtained upon irradiation in different regions of the solar spectrum. Reaction conditions: m_{cat} = 1 mg, $V_{reactor}$ = 3 mL, T = 25°C, t = 1 h. d) Proposed mechanism and e) scheme for the plasmon-assisted photocatalytic N_2 reduction. The transmittance results of used cut-off filters are shown in Figure S13 (Supporting Information).

O_2^- (solid lines, Figure 5a,b). This result points to the conclusion that, in the presence of N_2, the electrons generated in the activation of the conduction band of the TiO_2 were used in the reduction of this molecule to NH_3 (Figure 5e). Our results clearly show the importance of both Au and TiO_2 working in tandem, as either material component by itself does not achieve significant activity (Figure S4, Supporting Information). This reinforces the expected enhancement effect of the Au structure over the TiO_2 performance, and suggest a poor N_2 reduction capability of the Au surfaces, even when exciting strong plasmonic modes. As shown in Figure 5d, the formation of NH_3 from N_2 appears to be more energetically favored than ROS formation and thus proceeds alongside the formation of O_2 as a result of H_2O oxidation. The generated O_2 reacts with a portion of the NH_3 to produce nitrites and nitrates, as summarized in Table S4 (Supporting Information), thereby closing the photocatalytic cycle.

To investigate the wavelength dependence of photocatalytic NRR, experiments were conducted using optical filters and the results are presented in Figure 5c. When the SiO_2/AuNST/TiO_2/mSiO_2 hybrid catalyst was irradiated with light in the 360–517 nm range to selectively excite the gold interband transitions, NH_3 production reached 156.5 ± 8.9 μmol g_{cat}^{-1} h^{-1}. However, when the irradiation wavelength exceeds 500 nm, excitation is primarily confined to the Au LSPR, and NH_3 production slightly decreases to 134.6 ± 4.2 μmol g_{cat}^{-1} h^{-1}. These spectrally selective photodegradation were obtained using filters with an ≈90% transmittance at the relevant wavelengths (Figure S13, Supporting Information) We can therefore see the contributions arising from the excitation of both gold interband transitions and the semiconductor, at short wavelenghts, and the plasmonic excitation, at long wavelengths. Both of these groups of optical excitation channels contribute roughtly equally to the catalytic performance of the hybrid structures, indicating that in both spectral ranges the hybrid can advance both hemireactions.

For these materials to work in tandem to driving the redox hemireactions indicated in Figure 5d, the clear candidate for the driving mechanism would be the injection of excited "hot" charge carriers from the plasmonic material to the semiconductor, where they contribute to the redox reactions. This include

the injection of hot electrons excited from intraband transitions at the plasmonic band, the injection of hot holes due to both intraband and interband transitions, and even the injection of hot electrons due to interband transitions at wavelengths under ~400 nm due to the photon having sufficient energy to excite an electron from the d-band and still impart to it excess energy that allows its injection to the TiO_2 conduction band. In contrast, plasmonic near-field-driven enhancement of optical transitions in the TiO_2 cannot be significant because of the plasmon bands of all gold nanostructures occurring at longer wavelengths than those exciting the TiO_2 bandgap. Moreover, the small amount of local heating in our temperature-controlled experiment would not induce relevant population changes in the TiO_2 bands. Interestingly, the plasmon wavelength of our AuNST permits the injection of both excited electrons and holes into the TiO_2 conduction and valence bands, respectively. At high photon energies, interband transitions in Au will provide comparatively long-lived excited holes, while the overlapping tip and core plasmons of the AuNST will still provide energetic electrons through intraband transitions at wavelengths close to 500 nm. At the main plasmon peak, ≈650 nm, the photon energy can still be sufficient to promote through intraband transitions both electron and holes with enough excess energy to travel to the TiO_2. The high yields observed when using the two different excitation spectral ranges in Figure 5c strongly suggest that the reaction does not suffer from a significant bottleneck by either the reduction or oxidation paths in either of these spectral ranges.

3. Conclusion

In summary, Au/TiO_2 hybrid nanocomposites were successfully developed for the photocatalytic reduction of N_2 under visible light, achieving efficient NH_3 production. Among the morphologies evaluated, the nanocomposites incorporating AuNST demonstrated the highest photocatalytic activity, reaching 240 ± 10.5 μmol g_{cat}^{-1} h^{-1}. This exceptional performance is attributed to the strong localized electromagnetic fields generated around the spikes of the nanostructures. Furthermore, coating the nanoarchitecture with a mesoporous silica shell ensured structural stability, maintaining consistent performance over six consecutive cycles. Notably, ammonia formation was monitored in real-time using *operando* SERS spectroscopy. The Raman spectrum in the N–H stretching region displayed a wealth of signals associated with NH_3, providing detailed insights into the reaction dynamics. In addition, the wavelength dependence reveals a synergistic interplay between gold interband transitions and plasmonic effects, interfaced with the TiO_2 semiconductor, which enhances catalytic performance across the spectrum. Finally, to unravel the mechanism behind the photoreduction of N_2, the photogeneration of two key reactive oxygen species (ROS), the hydroxyl radical ($OH^{\cdot}$) and the superoxide radical (O_2^{-}), was examined. Control experiments revealed that while both ROS were detected in the presence of O_2, none of them was observed under N_2, indicating that the electrons generated in the conduction band of TiO_2 NPs were instead directed toward reducing N_2 to NH_3. This process is energetically favorable, with NH_3 formation occurring alongside H_2O oxidation to O_2, some of which reacts with NH_3 to produce nitrites and nitrates, thereby completing the photocatalytic cycle.[48–68]

Supporting Information

Supporting Information is available from the Wiley Online Library or from the author.

Acknowledgements

Y.N.-M. and A.S.-C. contributed equally to this work. B.P. and M.A.C.-D. acknowledge financial support from the Spanish Ministerio de Ciencia e Innovación under project TED2021-132101B-I00/AEI/10.13039/501100011033. M.A.C.-D. acknowledges financial support from Spanish Ministerio de Ciencia e Innovación under project PID2020-113704RB-I00/AEI/10.13039/501100011033, Xunta de Galicia/FEDER (IN607A 2018/5 and Centro Singular de Investigación de Galicia, Acc. 2019–2022, ED431G 2019-06). M.V.-G. and M.A.C.-D. acknowledge financial support from the Spanish Ministerio de Ciencia e Innovación under project PID2023-147495OB-I00. A.S.C. acknowledges Xunta de Galicia, Spain for her postdoctoral fellowship. B.P. acknowledges grant RYC2021-031910-I from Spanish Ministerio de Ciencia e Innovación and Excelencia-ED431F 2024/05 (Xunta de Galicia). R.A.A.-P. acknowledges financial support from Spanish Ministerio de Ciencia e Innovación under projects PID2023-152767NB-I00 and PID2020-120306RB-I00. L.V.B. acknowledges support under grant RYC2021-033818-I funded by MCIN/AEI/10.13039/501100011033. M.V.G. acknowledges grant RYC2022-038390-I from the Spanish Ministerio de Ciencia e Innovación. Y.N.-M. acknowledge financial support from the ministerio de Universidades (33.50.460A.752) and NextGeneration EU/PRTR under a Margarita Salas contract at Universidade de Vigo. Authors acknowledge the use of scientific and technical services from Centro de Apoio Científico e Tecnolóxico á Investigación (CACTI-Universidade de Vigo).

Conflict of Interest

The authors declare no conflict of interest.

Data Availability Statement

The data that support the findings of this study are available from the corresponding author upon reasonable request.

Keywords

ammonia, gold nanoparticles, hybrid photocatalyst, nitrogen reduction, plasmonic photocatalyst

Received: March 18, 2025
Revised: May 27, 2025
Published online: June 13, 2025

[1] L. Collado, A. H. Pizarro, M. Barawi, M. García-Tecedor, M. Libras, V. A. de la Peña O'Shea, *Chem. Soc. Rev.* **2024**, *53*, 11334.
[2] S. Linic, P. Christopher, D. B. Ingram, *Nat. Mater.* **2011**, *10*, 911.
[3] S. Linic, U. Aslam, C. Boerigter, M. Morabito, *Nat. Mater.* **2015**, *14*, 567.
[4] Z. Zhang, C. Zhang, H. Zheng, H. Xu, *Acc. Chem. Res.* **2019**, *52*, 2506.
[5] L. M. Liz-Marzán, *Langmuir* **2006**, *22*, 32.
[6] E. A. Monyoncho, M. Dasog, *Adv. Energy Sustainability Res.* **2021**, *2*, 2000055.
[7] C. Mao, J. Wang, Y. Zou, H. Li, G. Zhan, J. Li, J. Zhao, L. Zhang, *Green Chem.* **2019**, *21*, 2852.

[8] C. Li, T. Wang, Z. J. Zhao, W. Yang, J. F. Li, A. Li, Z. Yang, G. A. Ozin, J. Gong, *Angew. Chem., Int. Ed.* **2018**, *57*, 5278.
[9] G. C. Phan-Quang, X. Han, C. S. L. Koh, H. Y. F. Sim, C. L. Lay, S. X. Leong, Y. H. Lee, N. Pazos-Perez, R. A. Alvarez-Puebla, X. Y. Ling, *Acc. Chem. Res.* **2019**, *52*, 1844.
[10] M. Blanco-Formoso, N. Pazos-Perez, R. A. Alvarez-Puebla, *J. Raman Spectrosc.* **2021**, *52*, 554.
[11] M. Blanco-Formoso, N. Pazos-Perez, R. A. Alvarez-Puebla, *Nanoscale* **2020**, *12*, 14948.
[12] C. Burda, X. Chen, R. Narayanan, M. El-Sayed, *Chem. Rev.* **2005**, *105*, 1025.
[13] K. S. Lee, M. El-Sayed, *J. Phys. Chem.* **2005**, *109*, 20331.
[14] S. Dodson, M. Haggui, R. Bachelot, J. Plain, S. Li, Q. Xiong, *J. Phys. Chem. Lett.* **2013**, *4*, 496.
[15] N. W. Bigelow, A. Vaschillo, V. Iberi, J. P. Camden, D. J. Masiello, *ACS Nano* **2013**, *6*, 7497.
[16] E. Y. Santiago, L. V. Besteiro, X. T. Kong, M. A. Correa-Duarte, Z. Wang, A. O. Govorov, *ACS Photonics* **2020**, *7*, 2807.
[17] H. Wei, H. Xu, *Nanoscale* **2013**, *5*, 10794.
[18] Y. Gao, J. Wang, W. Wang, T. Zhao, Y. Cui, P. Liu, S. Xu, X. Luo, *Anal.Chem.* **2021**, *93*, 2480.
[19] J. Gargiulo, R. Berte, Y. Li, S. A. Maier, E. Cortes, *Acc. Chem. Res.* **2019**, *52*, 2525.
[20] L. Nan, J. Giráldez-Martínez, A. Stefancu, L. Zhu, M. Liu, A. O. Govorov, L. V. Besteiro, E. Cortes, *Nano Lett.* **2023**, *23*, 2883.
[21] J. W. Hong, D. H. Wi, S. U. Lee, S. W. Han, *J. Am. Chem. Soc.* **2016**, *138*, 15766.
[22] A. Sousa-Castillo, M. Comesaña-Hermo, B. Rodríguez-González, M. Pérez-Lorenzo, Z. Wang, X. T. Kong, A. O. Govorov, M. A. Correa-Duarte, *Phys. Chem. C* **2016**, *120*, 11690.
[23] C. Hanske, M. N. Sanz-Ortiz, L. M. Liz-Marzán, *Adv. Mater.* **2018**, *30*, 1.
[24] C. Li, Y. Jin, *Adv. Funct. Mater.* **2021**, *31*, 2008031.
[25] G. Decher, J. D. Hong, J. Schmitt, *Thin Solid Films* **1992**, *210–211*, 831835.
[26] Y. Negrín-Montecelo, A. H. A. Geneidy, A. O. Govorov, R. A. Alvarez-Puebla, L. V. Besteiro, M. A. Correa-Duarte, *ACS Photonics* **2023**, *10*, 3310.
[27] Y. Negrín-Montecelo, X. T. Kong, L. V. Besteiro, E. Carbó-Argibay, Z. M. Wang, M. Pérez-Lorenzo, A. O. Govorov, M. Comesaña-Hermo, M. A. Correa-Duarte, *ACS Appl. Mater. Interfaces* **2022**, *14*, 35734.
[28] W. L. Liu, F. C. Lin, Y. C. Yang, C. H. Huang, S. Gwo, M. H. Huang, J. S. Huang, *Nanoscale* **2013**, *5*, 7953.
[29] Y. Negrín-Montecelo, M. Testa-Anta, L. Marín-Caba, M. Pérez-Lorenzo, V. Salgueiriño, M. A. Correa-Duarte, M. Comesaña-Hermo, *Nanomaterials* **2019**, *9*, 1.
[30] A. Kumar, P. Choudhary, A. Kumar, P. H. C. Camargo, V. Krishnan, *Small* **2022**, *18*, 2101638.
[31] P. Yu, L. V. Besteiro, Y. Huang, J. Wu, L. Fu, H. H. Tan, C. Jagadish, G. P. Wiederrecht, A. O. Govorov, Z. Wang, *Adv. Opt. Mater.* **2019**, *7*, 1.
[32] E. Cortés, L. V. Besteiro, A. Alabastri, A. Baldi, G. T., A. Demetriadou, P. Narang, *ACS Nano* **2020**, *14*, 16202.
[33] E. Tiryaki, A. Sousa-Castillo, L. Rodríguez-Lorenzo, B. Espiña, R. A. Alvarez-Puebla, M. A. Correa-Duarte, *ChemCatChem* **2024**, *16*, 1.
[34] L. Yuan, C. Han, M. Pagliaro, Y. J. Xu, *J. Phys. Chem. C.* **2016**, *120*, 265.
[35] Y. Negrín-Montecelo, M. Comesaña-Hermo, L. K. Khorashad, A. Sousa-Castillo, Z. Wang, M. Pérez-Lorenzo, T. Liedl, A. O. Govorov, M. A. Correa-Duarte, *ACS Energy Lett.* **2020**, *7*, 778.
[36] S. Ezendam, M. Herran, L. Nan, C. Gruber, Y. Kang, F. Gröbmeyer, R. Lin, J. Gargiulo, A. Sousa-Castillo, E. Cortés, *ACS Energy Lett.* **2022**, *7*, 778.
[37] Y. Negrín-Montecelo, C. Brissaud, J. Y. Piquemal, A. O. Govorov, M. A. Correa-Duarte, L. V. Besteiro, M. ComesañaHermo, *Nanoscale* **2022**, *14*, 11612.
[38] B. Liu, Y. Jiang, Y. Wang, S. Shang, Y. Ni, N. Zhang, M. Cao, C. Hu, *Catal. Sci. Technol.* **2018**, *8*, 1094.
[39] G. W. Watt, J. D. Chrisp, *Anal. Chem.* **1952**, *24*, 2006.
[40] W. A. Senior, W. K. Thompson, *Nature* **1965**, *205*, 170.
[41] P. Cao, R. Gu, L. Qiu, R. Sun, B. Ren, Z. Tian, *Surf. Sci.* **2003**, *531*, 217.
[42] Y. Liu, T. Asset, Y. Chen, E. Murphy, E. O. Potma, I. Matanovic, D. A. Fishman, P. Atanassov, *iScience* **2020**, *23*, 1.
[43] R. Chellappa, D. Dattelbaum, L. Daemen, Z. Liu, *J. Phys.: Conf. Ser.* **2014**, *500*, 052008.
[44] S. Zhang, D. Chen, P. Chen, R. Zhang, Y. Hou, Y. Guo, P. Li, X. Liang, T. Xing, J. Chen, Y. Zhao, Z. Huang, D. Lei, Ch. Zhi, *Adv. Mater.* **2024**, *36*, 2310776.
[45] Y. Zhao, F. Li, W. Li, Y. Li, Ch. Liu, Z. Zhao, Y. Shan, Y. Ji, L. Sun, *Angew.Chem., Int. Ed.* **2021**, *60*, 20331.
[46] A. Sousa-Castillo, J. R. Couceiro, M. Tomás-Gamasa, A. Mariño-López, F. López, W. Baaziz, O. Ersen, M. Comesaña-Hermo, J. L. Mascareñas, M. A. Correa-Duarte, *Nano Lett.* **2020**, *20*, 7068.
[47] L. Marín-Caba, G. Bodelón, Y. Negrín-Montecelo, M. A. Correa-Duarte, *Adv. Funct. Mater.* **2021**, *31*, 2105807.
[48] W. Stober, A. Fink, D. E Bohn, *J. Colloid Interface Sci.* **1968**, *26*, 62.
[49] J. Turkevich, P. C. Stevenson, J. Hillier, *Discuss. Faraday Soc.* **1951**, *11*, 55.
[50] P. Senthil Kumar, I. Pastoriza-Santos, B. Rodríguez-González, F. Javier García De Abajo, L. M. Liz-Marzán, *Nanotechnology* **2008**, *19*, 1.
[51] L. Scarabelli, A. Sánchez-Iglesias, J. Pérez-Juste, L. M. Liz-Marzán, *J. Phys. Chem. Lett.* **2015**, *6*, 4270.
[52] S. Leichnitz, J. Heinrich, N. Kulak, *Chem. Commun.* **2018**, *54*, 13411.
[53] Y. Nosaka, A. Y. Nosaka, *Chem. Rev.* **2017**, *117*, 11302.
[54] Bran and Luebbe, Method No. G-172-96, Bran+Luebbe Inc., Buffalo Grove, IL, USA, **1999**.
[55] C. Xiao, H. Hu, X. Zhang, D. R. MacFarlane, *ACS Sustainable Chem. Eng.* **2017**, *5*, 10858.
[56] J. Yang, Y. Guo, R. Jiang, F. Qin, H. Zhang, W. Lu, J. Wang, J. C. Yu, *J. Am. Chem. Soc.* **2018**, *140*, 8497.
[57] H. Jia, A. Du, H. Zhang, J. Yang, R. Jiang, J. Wang, C.-Y. Zhang, *J. Am. Chem. Soc.* **2019**, *141*, 5083.
[58] C. Hu, X. Chen, J. Jin, Y. Han, S. Chen, H. Ju, J. Cai, Y. Qiu, C. Gao, C. Wang, Z. Qi, R. Long, L. Song, Z. Liu, Y. Xiong, *J. Am. Chem. Soc.* **2019**, *141*, 7807.
[59] Y. Guo, J. Yang, D. Wu, H. Bai, Z. Yang, J. Wang, B. Yang, *J. Mater. Chem. A* **2020**, *8*, 16218.
[60] S. Wu, Z. Chen, K. Liu, W. Yue, L. Wang, J. Zhang, *ChemSusChem* **2020**, *13*, 3455.
[61] Y. Chang, D. Guo, L. Wu, B. Li, J. Yang, *Chem. Sci.* **2021**, *12*, 11213.
[62] P. Qiu, C. Huang, G. Dong, F. Chen, F. Zhao, Y. Yu, X. Liu, Z. Li, Y. Wang, *J. Mater. Chem. A* **2021**, *9*, 14459.
[63] L.-W. Chen, Y.-C. Hao, Y. Guo, Q. Zhang, J. Li, W.-Y. Gao, L. Ren, X. Su, L. Hu, N. Zhang, S. Li, X. Feng, L. Gu, Y.-W. Zhang, Z.-X. Yin, B. Wang, *J. Am. Chem. Soc.* **2021**, *143*, 5727.
[64] H. Jia, F. Li, Y. Yang, M. Zhao, J. Li, C.-Y. Zhang, *Chem. Sci.* **2023**, *14*, 5656.
[65] J. S. Prabagar, K. L. Reddy, D.-K. Lim, *Chin. J. Struct. Chem.* **2025**, *44*, 100564.
[66] Q. Dong, X. Li, Y. Duan, X. He, X. Liang, F. Yu, C. Wang, *Appl. Catal., B Environ. Energy* **2025**, *366*, 125042.
[67] Y. Yang, H. Jia, N. Hu, M. Zhao, J. Li, W. Ni, C.-Y. Zhang, *J. Am. Chem. Soc.* **2024**, *146*, 7734.
[68] H. Huang, S. Wang, X. Fan, D. Philo, L. Fang, W. Tu, T. Qiu, Z. Zou, J. Ye, *ACS Sustainable Chem. Eng.* **2023**, *11*, 10993.